Eur. Phys. J. E (2019) **42**: 121
DOI 10.1140/epje/i2019-11887-6

THE EUROPEAN PHYSICAL JOURNAL E

Regular Article

Relaxation dynamics and crystallization study of glass-forming chiral-nematic liquid crystal S,S-2,7-bis(4-pentylphenyl)-9,9-dimethylbutyl 9H-fluorene (5P-Am*FLAm*-P5)*

Małgorzata Jasiurkowska-Delaporte[1,a], Tomasz Rozwadowski[1], Ewa Juszyńska-Gałązka[1], Jan Krawczyk[1], Ewelina Dmochowska[2], Przemysław Kula[2], and Maria Massalska-Arodź[1]

[1] Institute of Nuclear Physics, Polish Academy of Sciences, ul. Radzikowskiego 152, 31-342 Kraków, Poland
[2] Institute of Chemistry, Military University of Technology, Warsaw, Poland

Received 27 May 2019 and Received in final form 8 August 2019
Published online: 11 September 2019

Abstract. The chiral nematic S,S-2,7-bis(4-pentylphenyl)-9,9-dimethylbutyl9H-fluorene (5P-Am*FLAm*-P5) liquid crystal shows a complex phase diagram strongly dependent on thermal treatment as identified by Polarizing Optical Microscopy (POM) and differential scanning calorimeter (DSC). The molecular dynamics in various thermodynamics states was studied by means of broadband dielectric spectroscopy (BDS). The vitrification of a chiral nematic phase (N*) is manifested by a Vogel-Fulcher-Tammann (VFT)-type temperature dependence of structural relaxation time (τ_α). Three dielectric relaxation processes exhibiting Arrhenius-like thermal activation were found in conformationally disordered (condis) Cr1 and Cr2 structures. The isothermal cold crystallization process of Cr2 occurs in the metastable N* phase; however, in the non-isothermal experiments, the Cr2 phase is formed in the isotropic phase obtained on heating the metastable N* phase. The findings for the isothermal process were compared with those regarding non-isothermal crystallization.

1 Introduction

Vitrification and crystallization phenomena play an important role in industry, particularly in processes associated with drug stability [1], polymer production [2] and food preservation [3]. Upon cooling to just below the melting temperature, some materials form a crystal structure, with their molecules distributed throughout a crystalline lattice; this state is characterized by unique physical properties. As crystallization takes some time, first for the creation of small nuclei throughout the sample and then for crystal growth, many substances can be supercooled to a glass state [4]. The potential for a liquid to crystallize or vitrify depends on both external factors and the microscopic properties of the material, these being its molecular structure, chemical bonds and intermolecular interactions [5]. As the stable crystalline phase has lower free energy than the glass state, a metastable disordered liquid in glass form can transform into a crystal upon heating: a process called *cold crystallization* [6]. This process differs from *melt crystallization* [7]: the typical crystallization process which takes place on cooling at higher temperatures. The ability to control cold crystallization is very important for thermal energy storage, as stored heat is released by cold crystallization on re-heating [8]. However, the crystallization process can occur differently under isothermal and non-isothermal conditions [9], and so both kinds of experiments are necessary to reveal the full crystallization pattern of a substance.

A characteristic feature of glass formation is that the viscosity increases by several orders of magnitude, up to 10^{13} poise, when approaching T_g, resulting in lower fluidity and apparent rigidity [10]. On approaching T_g, the dynamic cooperativity of the dipolar molecules increases, resulting in the occurrence of structural α-relaxation deviating from Arrhenius behavior; it is rather described in terms of the free volume model based on the Vogel-Fulcher-Tammann (VFT) relationship [11]:

$$\tau_\alpha = \tau_\infty \exp\left(\frac{D_f T_0}{T - T_0}\right),$$

where τ_∞ is the so-called pre-exponential factor, D_f is a constant and T_0 denotes the Vogel temperature.

* Contribution to the Topical Issue "Dielectric Spectroscopy Applied to Soft Matter" edited by Simone Napolitano.

[a] e-mail: Malgorzata.Jasiurkowska-Delaporte@ifj.edu.pl

A measure of how well a glass-forming system adapts to temperature change is the fragility index m_f, defined by the slope at T_g in a plot of $\log(\tau_\alpha)$ *vs.* T_g/T [11–13]. The fragility of the substance is related fundamentally to the thermodynamic [14] and structural properties of materials [15]. In addition, in glasses, m_f is also proportional to the intensity of the so-called *boson peak* related to damped low-energy excitations (with non-zero lasting time), as opposed to the regular phonons identified in crystals [16]. Angell proposes that glasses can be classified into two groups based on m_f: strong glasses with m_f of ~ 16, and fragile glasses with larger values of m_f up to 200. It was recently found that m_f also determines the probability of the appearance of a crystalline phase in a supercooled liquid in the process of cold crystallization [17], *i.e.* fragile glass formers show a high tendency to crystallize upon heating. Moreover, Egider [18] demonstrated that m_f can be used to predict the coupling coefficient (ξ) between α-relaxation time and crystallization growth kinetics.

Glasses were initially understood as amorphous solids with some degrees of freedom frozen-in [19]. Gradually, the definition of a vitreous state expanded to embrace a partially ordered glass formed by the cooling of an orientationally disordered crystal (ODIC) [20], characterized by a substance whose molecules are disorientated despite having their centers distributed regularly through the crystalline lattice, and nematic liquid crystals [21–23], consisting of randomly distributed molecules with long molecular axes tending to align parallel to each other. Also, some smectic phases, such as smectic E [24–27], smectic B [28,29] and smectic G [30], form partially ordered glasses. Recent studies have also examined the vitrification of crystalline phases characterized by both orientational and conformational degrees of freedom (condis type of glass) [31,32].

Cold crystallization in liquid crystals (LCs) was first demonstrated by BDS studies for chiral isooctyloxycyanobiphenyl [22]. Further investigations into crystallization phenomena in LCs indicated that they depend on the degree of order of the initial phase and the thermal history of the sample. Two different mechanisms were identified for non-isothermal cold crystallization in 4CFPB glass-forming LC [33]: for slower heating at low temperatures, the crystallization of the metastable nematic phase is controlled by diffusion, while for faster heating at higher temperatures, the key role is played by the thermodynamic driving force. The opposite scenario was revealed for the non-isothermal melt crystallization in the smectic-B phase of the BBOA liquid crystal [9]. Our recent paper comparing the melt and cold isothermal crystallization in a glass-forming non-chiral 5P-EtFLEt-P5 liquid crystal found that the melt crystallization processes occur more quickly than the cold ones; this was attributed to the fact that the molecular order in the nematic state (N) upon cooling was higher than that of the metastable nematic state obtained after softening of the glass [23]. However, further systematic studies of other substances are required to understand the relationship between the structure of LC phases and the kinetics of its crystallization.

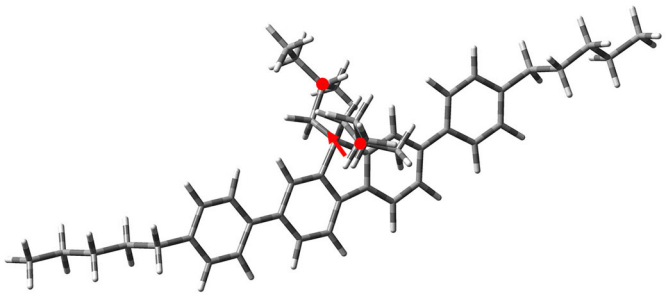

Fig. 1. Structure of S,S-2,7-bis(4-pentylphenyl)-9,9-dimethylbutyl 9H-fluorene (5P-Am*FLAm*-P5). The geometry of the lowest-energy conformation of the molecule optimized by the Hartree-Fock (HF) method. The arrow presents the direction of the resultant dipole moment of about 0.32 D. The stereocenter of the molecule is denoted by dots.

The current contribution characterizes the molecular dynamics of 5P-Am*FLAm*-P5 (see fig. 1), a newly synthetized chiral substance with the same molecular core as 5P-EtFLEt-P5, in the chiral nematic N* vitreous state, *i.e.* the metastable N* phase observed after softening of the glass, as well as in the crystalline phases. The phase diagram was revealed by polarized optical microscopy (POM). Special emphasis was given to the kinetics of the crystallization process taking place under isothermal and non-isothermal conditions, investigated by a combination of differential scanning calorimetry and broadband dielectric spectroscopy. Finally, the paper discusses the coupling between the characteristic crystallization times and the α-relaxation rates of the compound, as well as its thermodynamic properties.

2 Experimental

2.1 Synthesis of 5P-Am*FLAm*-P5

The high-purity ($> 99\%$) 5P-Am*-FL-Am*-P5 compound was synthesized at the Institute of Chemistry at the Military University of Technology, Warsaw, Poland. The general synthesis pathway of S,S-2,7-bis(4-pentylphenyl)-9,9-dimethylbuthyl-9H-fluorene is shown in fig. 2. The purity of the synthesised material, and its synthesis, was monitored by thin-layer chromatography and a Shimadzu GCMS-QP2010S gas chromatograph equipped with quadrupole mass analyser (MS). The synthesis of the final compound consisted of three stages. In the first step, fluorene (commercially available) was halogenated with bromine-iodine mixture to 2,7-dibromofluorene; following this, the compound was subjected to nucleophilic substitution with (S)-1-bromo-2-methylbutane to obtain laterally substituent fluorene derivatives in the 9,9 positions. Finally, the main product 5P-Am*-FL-Am*-P5 was obtained by a Suzuki-Miyaura cross-coupling reaction between S,S-2,7-dibromo-9,9-dimethylbythyl-9H-fluorene and (4-pentylphenyl)boronic acid.

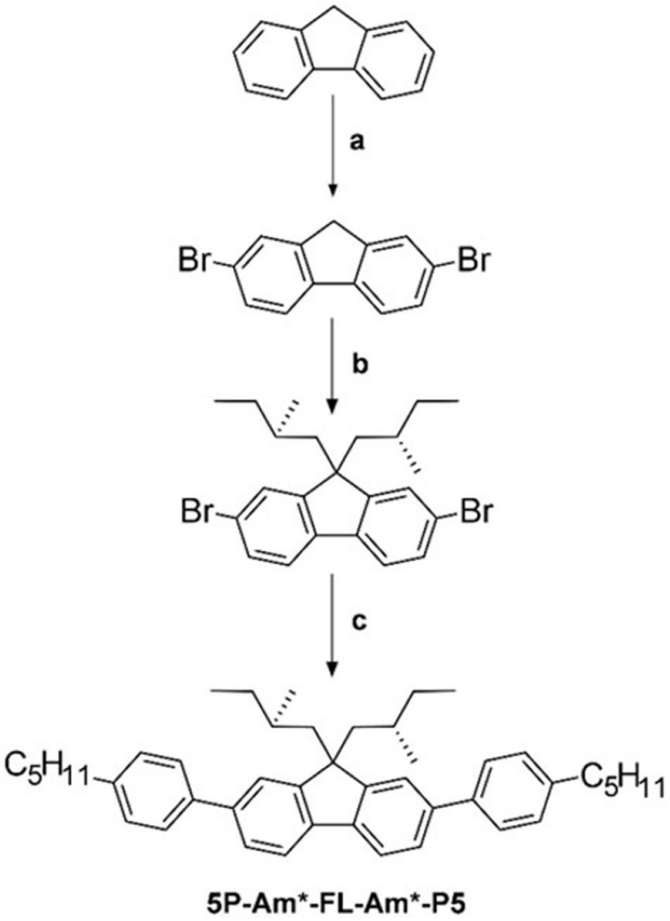

Fig. 2. Synthesis of compound 5P-Am*-FL-Am*-P5. Conditions of stages: (a) I_2, Br_2, $NaHSO_3/H_2O$, CH_2Cl_2; (b) (S)-1-bromo-2-methylbutane, KOH, KI, DMSO; (c) (4-pentylphenyl)boronic acid, K_2CO_3, $Pd(OAc)_2$, acetone/H_2O.

2.2 Broadband Dielectric Spectroscopy (BDS)

To perform BDS measurements, 5P-Am*FLAm*-P5 powder was heated to an isotropic phase; the sample was heated between two circular electrodes with a diameter of 10 mm, which were separated by Teflon spacers to avoid a short circuit. The dielectric spectra (ε^*) were measured every 2 K using a high-resolution Novocontrol Alpha Analyzer (10^{-1} Hz–10^7 Hz) in the temperature range 173 K–400 K upon cooling and heating. The analyser was supported by a Novocool temperature controller providing temperature stability better than 0.1 K.

The relaxation times were determined by fitting the complex dielectric spectra with the empirical Havriliak-Negami function given by

$$\varepsilon^*(\omega) = \varepsilon'(\omega) - i\varepsilon''(\omega) = \varepsilon_\infty + \sum_{k=1}^{2} \frac{\Delta\varepsilon_k}{(1+(i\omega\tau_{HN_k})^{a_{HN_k}})^{b_{HN_k}}} + \frac{\sigma_0}{\omega\varepsilon_0}, \quad (1)$$

where ε' and ε'' are the real and imaginary parts of the complex dielectric function, $\Delta\varepsilon_i$ and τ_{HNi} are the dielectric strength and the macroscopic relaxation time of process k, σ_0 is a dc-conductivity. The fitting parameters a_{HN}, and b_{HN} describe the shape of the loss spectra in comparison to the Debye limit with a_{HN}, $b_{HN} = 1$. The a_{HN} and b_{HN} values are related to the limiting behaviour of the complex dielectric function at low and high frequencies:

$$\varepsilon'(0) - \varepsilon'(\omega) \sim \omega^m; \quad \varepsilon'' \sim \omega^m \quad \text{for } \omega \ll 1/\tau_{HN} \text{ with } m = a_{HN}, \quad (2)$$

$$\varepsilon'(\omega) - \varepsilon'_\infty \sim \omega^{-n}; \quad \varepsilon'' \sim \omega^{-n} \quad \text{for } \omega \gg 1/\tau_{HN} \text{ with } n = a_{HN}b_{HN}, \quad (3)$$

where $\varepsilon'(0)$ and ε'_∞ describe the value of ε' at the low and high frequency limit, respectively. The n and m parameters give information about the local and long-range correlations of the reorienting molecules, respectively.

2.3 Differential Scanning Calorimetry (DSC)

DSC curves were measured for various cooling/heating rates for a 6.16 mg sample by means of a DSC 2500 Differential Scanning Calorimeter (TA Instruments). The LC substance, as received, was placed in an aluminum pan. Prior to the first measurement sequence, the sample was heated up to an isotropic state at 400 K and kept at this temperature for five minutes. The set-up is equipped with a cooling system using liquid nitrogen. Heat flow *vs.* furnace temperature is determined as the difference between the "heat flux" observed in the material placed in the Tzero aluminum hermetic pan and an empty aluminum pan used as a reference. The temperature and heat flow calibration of the equipment was determined before measurements using an indium reference material. The measurement sensitivity of heat flow was better than 0.2 μW on the same sensor operating across the full temperature range. The accuracy of temperature determination was not lower than $\pm 0.025\,^\circ$C, and the precision of temperature determination was not lower than $\pm 0.002\,^\circ$C. Baseline flatness (-50 to 300 °C) was $\leq 5\,\mu$W and baseline repeatability (-50 to 300 °C) $< 10\,\mu$W. By integrating the peak of the DSC thermograms corresponding to the phase transition, the change of enthalpy of the process, ΔH can be calculated as follows:

$$\Delta H = \int_{T_0}^{T_\infty} \frac{\Delta Q}{\Delta t}\frac{\Delta t}{\Delta T}\mathrm{d}T, \quad (4)$$

where $\Delta Q/\Delta t$ is the difference in the levels of thermal power delivered to the can with the sample and to the reference can, $\Delta T/\Delta t$ is a (constant in time) rate of temperature, T_0 and T_∞ are the temperatures of the beginning and the end of the observed DSC anomaly. Based on the enthalpy of the phase transition (in general, of the thermal anomaly), given by eq. (4), and the temperature T_p at which the phase transition occurs, the entropy change ΔS of the observed phase transition can be calculated as

$$\Delta S = \frac{\Delta H}{T_p}. \quad (5)$$

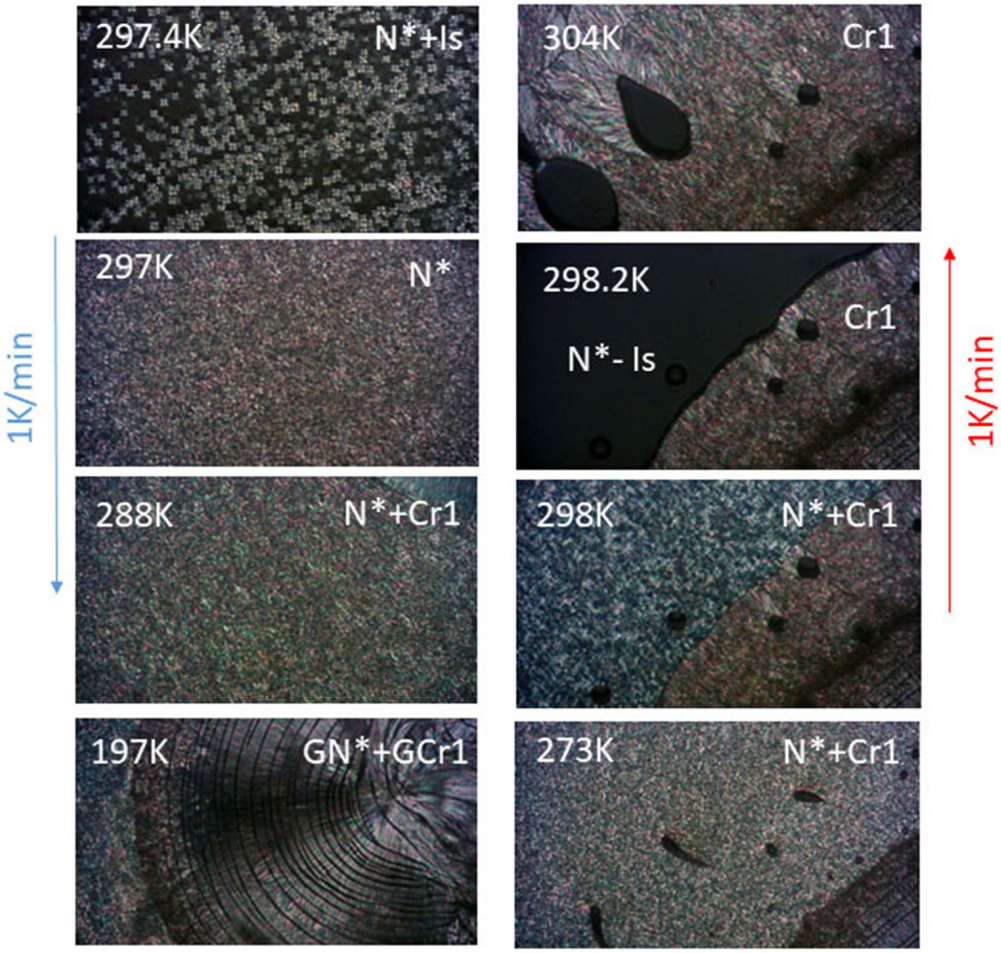

Fig. 3. Phase sequence of 5P-Am*FLAm*-P5 upon cooling and heating at a rate of 1 K/min as seen by POM.

2.4 Polarizing Optical Microscopy (POM)

The temperature changes of the textures were monitored by a Biolar PI polarizing light microscope in combination with a Linkam THM600 heating stage. The temperature of the sample was controlled with a high degree of accuracy (±0.1 K) using a flow of liquid nitrogen. The substance was placed on the glass and heated up to an isotropic state to ensure a uniform LC layer, and then was covered by a glass cover. The thickness of the material layer was determined as the difference between the total thickness of sandwich sample, measured by a high-precision micrometer screw, and the thickness of the glass covers. Thus the thickness of the sample layer was calculated as about 50 μm.

3 Results and discussion

3.1 Phase diagram

POM observations of texture alterations with temperature changes in 5P-Am*FLAm*-P5 revealed its complex phase diagram and strong dependence on the cooling/heating rate. Upon slow cooling (1 K/min), some portion of the chiral nematic N* (N*) was found to undergo transformation to Cr1 phase at 288 K (see fig. 3). Cracks appeared on the texture at low temperatures, then disappeared upon heating around 273 K; this was followed by a transformation of the N* phase to the isotropic state (Is), then the Is phase immediately crystallized to Cr1 at 304 K. Previously, similar cracking behavior was found for vitrification other materials [26,34–36], and we propose the following phase sequence on cooling: Is-Cr1, GCr1 (glass of Cr1). In the case of fast cooling, a small volume of the isotropic phase first forms another crystal Cr2 at 300 K; following this, the transition Is-N* and formation of the glass of N* (GN*) occur in the presence of Cr2 (fig. 4). Upon subsequent heating, softening of GN*, clearing and full crystallization of Cr2 in a metastable isotropic phase are observed, resulting in the melting of the Cr2 phase at 375 K: GN*-N*-Is-Cr2-Is.

Figure 5(a), (b) presents the temperature dependence of heat flow measured for 5P-Am*FLAm*-P5. Upon cooling at a rate of 1 K/min from the isotropic phase a jagged, broad peak was observed in the temperature range between 326 K and 313 K; this resulted in the co-existence of the Cr1 and N* phases, as identified in POM studies. Although upon cooling, the DSC thermogram does not

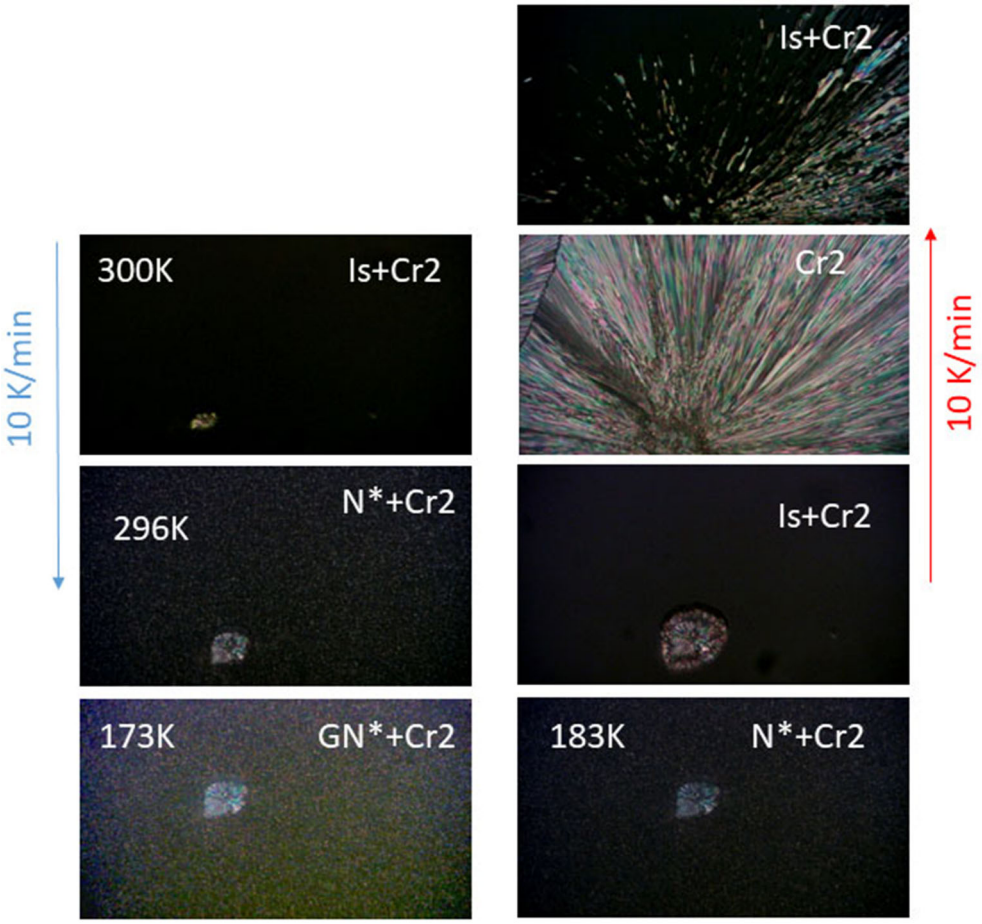

Fig. 4. Phase sequence of 5P-Am*FLAm*-P5 upon cooling and heating at a rate of 10 K/min as seen by POM.

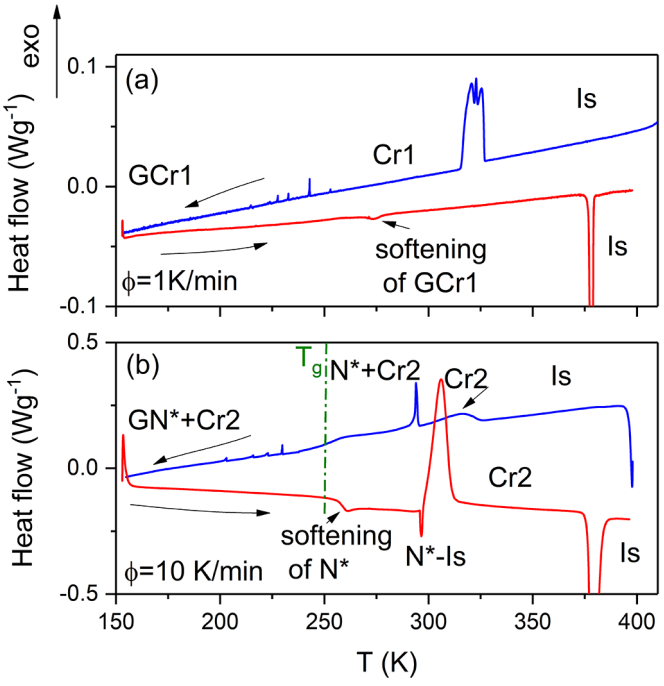

Fig. 5. Thermograms of 5P-Am*FLAm*-P5 obtained upon cooling and heating at a rate of (a) 1 K/min and (b) 10 K/min.

display a step-like change characteristic of the vitrification process, small needle-like peaks at low temperatures can be seen that indicate cracking of the sample; these are also revealed by microscopic examination of the physical textures (see image at 197 K in fig. 3). Such cracking is expected in the glassy state due to tension in material [37]. Upon subsequent heating, an anomaly related to the softening of GCr1 was observed around 273 K which coincides with the disappearance of cracks in POM textures. Following this, Cr1 fusion was observed at 378 K.

In the case of fast cooling (10 K/min), the DSC trace revealed a broad exothermic peak at around 315 K, ascribed to the partial crystallization of the isotropic phase to Cr2, a peak at about 294 K, attributed to the Is-N* transition, and a step-like change at 250 K, reflecting the vitrification of N* phase. Also, several spiky peaks were observed in the DSC curve for the glassy state of nematic phase (GN*). Following this, when the material was heated up, a transition was observed between the metastable nematic N* phase (after softening of N* glass) to an isotropic phase (N*-Is), as reflected by a sharp endothermic peak at 296.7 K, followed by the cold crystallization of Cr2 at 306 K. The observed differences in the temperatures of the phase transitions upon cooling are caused by different cooling rates.

Table 1. Thermodynamic quantities associated with the phase transitions of 5P-Am*FLAm*-P5.

Phase transition	T_{trs} [K]	$\Delta_{trs}H$ [kJ mol^{-1}]	$\Delta_{trs}S$ [J mol^{-1} K^{-1}]
Cooling 10 K/min			
I-Cr2	315.5	2.4	7.7
I-N*	294.1	1.2	4.1
Heating 10 K/min			
Cold crystallization of Cr2	–	–	–
Cr2-Is	379.4	25.9	68.4
Cooling 1 K/min			
Jagged, broad peak between 326 K and 313	–	–	–
Heating 1 K/min			
Cr1-Is	378.6	26.2	69.1

The temperature (T_{trs}), enthalpies ($\Delta_{trs}H$), and entropies ($\Delta_{trs}S = \Delta_{trs}H/T_{trs}$) associated with the phase transitions calculated according to eqs. (4) and (5) are reported in table 1. The fusion entropy values of the Cr1 and Cr2 crystals are similar, indicating that the two crystals have similar degrees of order.

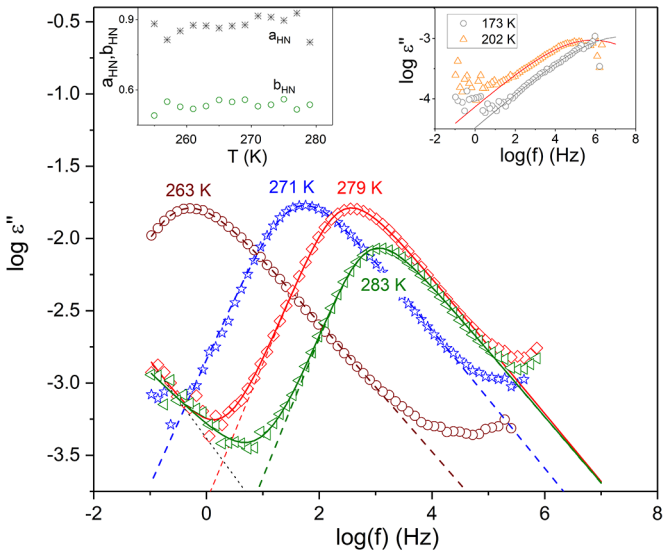

Fig. 6. Frequency-dependent dielectric loss of 5P-Am*FLAm*-P5 for selected temperatures obtained upon heating after fast cooling (15 K/min). The lines indicate fits to the data according to the Havriliak-Negami functions. The dashed lines and dotted lines correspond to the contribution from dielectric processes and electric conductivity, respectively in the N* phase. The left inset presents the temperature dependence of the shape parameters of the α-relaxation process. The right inset shows the secondary relaxation process in GN*. The error bars are smaller than the symbols, if not explicitly stated otherwise.

3.2 Molecular dynamics studies

BDS studies allow the thermodynamic phases in 5P-Am*FLAm*-P5 to be characterized in terms of dynamical features. Figure 6 presents dielectric absorption spectra $\varepsilon''(f)$ measured for the glass N* and the metastable N* phase obtained through softening of GN* on heating after fast cooling. The shape parameters (a_{HN}, b_{HN}) of the α-relaxation process (ascribed to reorientation of the molecules around the short axis), obtained by fitting the data by Havriliak-Negami relaxation function (eq. (1)), are temperature insensitive; their values indicate that the observed α-relaxation is of a non-Debye nature. The local and long-range correlations of 5P-Am*FLAm*-P5 molecular reorientations described by $n = a_{HN}b_{HN} \sim 0.45$ and $m = a_{HN} \sim 0.9$ are very strong. Two secondary β and γ processes are attributed, respectively, to the small-angle rotational diffusion of molecules around the short axis and to librations around the long axis, analogously to non-chiral 5P-EtFLEt-P5 liquid crystal with the same molecular core [23].

The relaxation process (I) measured in the Cr1 phase appears as a shoulder overlapped by a conductivity contribution (see fig. 7(a)). To extract the relaxation rate for his process, the data were analysed according to an approach proposed by Wübbenhorst and Turnhout [38,39]. This method is based on the assumption

$$\varepsilon''_{der} = -\frac{\pi\partial\varepsilon'(\omega)}{2\partial\ln\omega} \approx \varepsilon''. \qquad (6)$$

The derivative loss spectra $\varepsilon''_{der}(f)$ were fitted with the analytical derivative of the Havriliak-Negami function $\partial\varepsilon'_{HN}/\partial\ln\omega$. An example of deconvoluted spectrum in Cr1 is presented in fig. 7(b). The second relaxation process (II) in Cr1, observed in the low temperature range, is more pronounced in the temperature than the frequency domain. Thus, the relaxation rates of this process were determined from the maximum of dielectric loss *versus* temperature $\varepsilon''(T)$ at a selected frequency. The value of $\varepsilon''(T)$ maximum was designated by fitting a Gaussian to the data. The utility of this approach is described in refs. [40, 41]. To reveal the relaxation pattern in the Cr2 phase, the material was first cooled at a rate of 10 K/min to the GN* state, following which the Cr2 crystal was obtained by annealing at 275 K. The dielectric loss spectrum $\varepsilon''(f)$, deconvoluted into two components in the Cr2 phase, is shown in fig. 7(c).

Figure 8 displays the relaxation rates of all molecular processes in an Arrhenius presentation. The α-relaxation in the metastable N* phase fulfils the VFT temperature relationship. The temperature dependence of the dielectric increment ($\Delta\varepsilon$) is shown in the inset of fig. 8. The fitting parameters are reported in table 2. The secondary β and γ relaxations are Arrhenius-like, as are the processes in the crystalline phases. In the Cr2 phase, the low-temperature process (II) observed in the Cr1 crystal splits into two processes, which suggests that the degree of anisotropy of molecular motions increases [39]. Due to

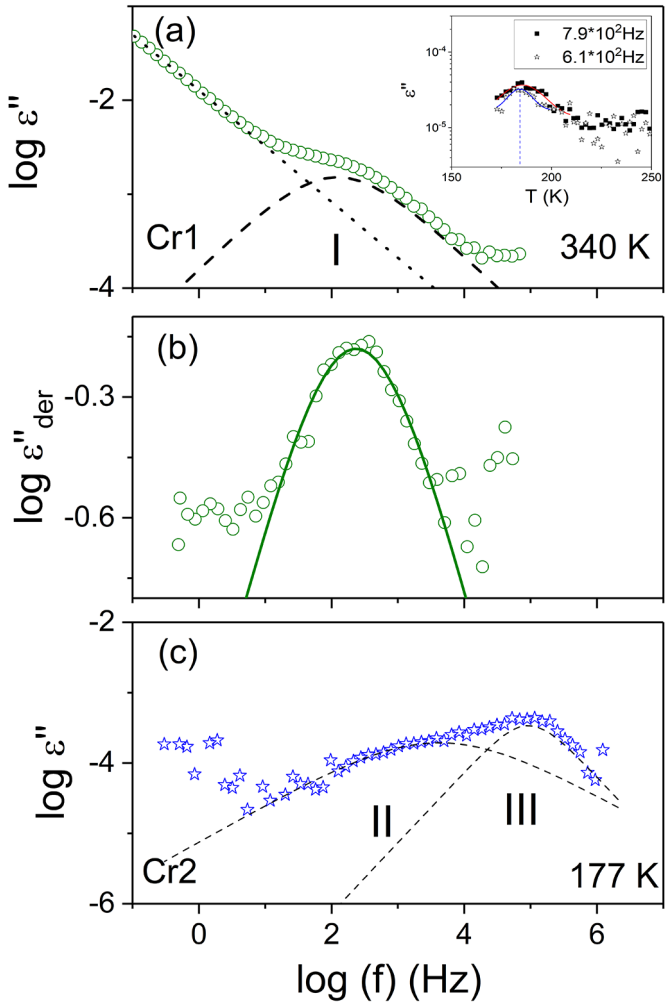

Fig. 7. (a) An example dielectric loss spectrum $\varepsilon''(f)$ measured in the Cr1 at 340 K upon cooling. The inset shows the imaginary part of the dielectric function *vs.* temperature. (b) The fit of derivative loss spectra $\varepsilon''_{der}(f)$. (c) $\varepsilon''(f)$ spectrum obtained in Cr2 phase at 177 K. To obtain the Cr2 phase, the sample was cooled from an isotropic state to the glass N* phase, then heated up to metastable N* phase and annealed for several hours at 275 K, following which it was then annealed for several hours.

Table 2. The VFT fitting parameters τ_α, fragility index m_f, and dielectric glass-transition temperature according to the convention $T_g = T(\tau_\alpha = 100\,\mathrm{s})$.

VFT parameters	
τ_∞	$3 * 10^{-12}$ s
D_f	5.8 ± 1.4
T_0	210 ± 3 K
m_f	117 ± 6
T_g (BDS)	248 ± 5 K

the efficient packing in the crystalline phases, as evidenced by the high value of the fusion entropy ($\Delta S_{\mathrm{Cr1\text{-}I,Cr2\text{-}I}} \approx 69\,\mathrm{kJ\,mol^{-1}\,K^{-1}}$), the molecular movements are strongly

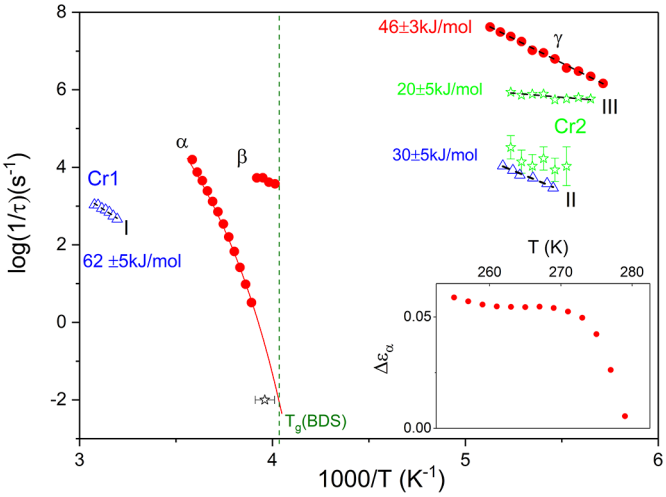

Fig. 8. Thermal activation plot of the α- and secondary relaxation process for 5P-Am*FLAm*-P5. The solid line represents the fit by the VFT equation to the relaxation rate $\log(1/\tau_\alpha)$ *vs.* $1/T$ in the N* phase. The dashed line indicates that of the Arrhenius equation fitted to the relaxation data in the Cr1 phase. The inset shows the temperature dependence of the dielectric strength $\Delta\varepsilon_\alpha$. The solid symbols indicate the secondary relaxation related to the dynamics responsible for the glass transition observed upon heating after fast cooling (15 K/min). The open symbols indicate relaxation rates obtained upon cooling in the crystalline form Cr1. The error bars are smaller than the symbols, if not explicitly stated otherwise.

restricted. This can be rationalized by the concept of conformationally disordered crystals (condis). Regarding the structure of 5P-Am*FLAm*-P5 molecules and the position of the resultant molecular dipole moment, the motions identified in Cr1 and Cr2 were attributed to small twisting movement of fluorene groups. The high molecular packing also favors the collective behavior. To support our hypothesis, the activation entropy ($\Delta S^{\#}$) and activation enthalpy ($\Delta H^{\#}$) of the relaxation processes were calculated according to the method proposed by the Starkweather [42]. In this approach $\Delta S^{\#}$ and $\Delta H^{\#}$ are given as

$$\Delta S^{\#} = \frac{1}{T'}\left[E_a - RT'\left(1 + \ln\frac{k_B T'}{2\pi h f}\right)\right], \tag{7}$$

$$\Delta H^{\#} = E_a - RT', \tag{8}$$

where T' is the temperature of the maximum of the relaxation peak at the selected reference frequency f ($f = 1$ Hz), E_a is an activation energy of the process, k_B is the Boltzmann constant and h denotes the Planck constant. The obtained positive values of $\Delta S^{\#}$ and $\Delta H^{\#}$ for the processes II ($\Delta S^{\#} = 0.17\,\mathrm{kJ\,mol^{-1}\,K^{-1}}$, $\Delta H^{\#} = 28.8\,\mathrm{kJ\,mol^{-1}}$) and III ($\Delta S^{\#} = 0.21\,\mathrm{kJ\,mol^{-1}\,K^{-1}}$, $\Delta H^{\#} = 19.3\,\mathrm{kJ\,mol^{-1}}$) confirm the cooperativity of the molecular motions in the crystalline phases.

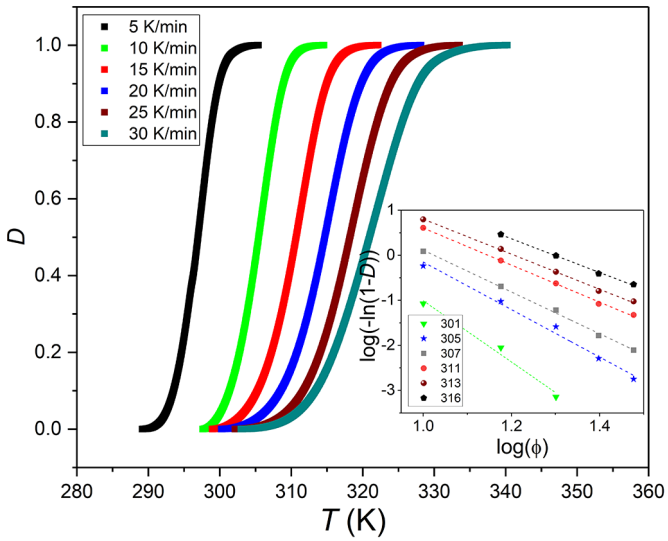

Fig. 9. The crystallization degree $D(T)$ *vs.* temperature determined from DSC measurements with different heating rates (ϕ). The inset shows Ozawa plots.

3.3 Kinetics of cold crystallization of Cr2 in 5P-Am*FLAm*-P5 under non-isothermal conditions

As presented above, upon heating at 10 K/min, the vitrified N* phase first softens and a metastable nematic N* undergoes a transition to an isotropic phase at 296 K; this finally crystallizes to Cr2 at 306 K. To recognize the tendency of 5P-Am*FLAm*-P5 to undergo cold crystallization under non-isothermal conditions, the kinetics of the non-isothermal crystallization of Cr2 was studied for various heating rates (ϕ) using the DSC technique. The relative degree of the non-isothermal crystallization (D) as a function of temperature is defined as [43]

$$D(T) = \frac{\int_{T_0}^{T} (\frac{\mathrm{d}H}{\mathrm{d}T})\mathrm{d}T}{\int_{T_0}^{T_\infty} (\frac{\mathrm{d}H}{\mathrm{d}T})\mathrm{d}T}, \qquad (9)$$

where $\mathrm{d}H/\mathrm{d}T$ is the heat flow, T_0 and T_∞ denote the points at which the crystallization process respectively starts and ends. Temperature dependences of the crystallization degree $D(T)$ determined from DSC measurements are presented in fig. 9. To gain more information about non-isothermal crystallization, the data were analyzed using the Ozawa equation which is a modified form of the Avrami model [44]

$$\log(-\ln(1-D)) = \log Z(T) - n_O \log(\phi), \qquad (10)$$

where D is the relative degree of non-isothermal crystallization, n_O is the Ozawa exponent related to the dimensionality of the crystal and $Z(T)$ is the Ozawa crystallization rate. For fixed temperatures, the plots of $\log(-\ln(1-D))$ as a function of $\log(\phi)$ are linear, with the slope being the parameter n_O and the intercept with the y-axis corresponding to $\log(Z(T))$ (inset of fig. 9). It was found that n_O decreases from 6.1 to 3.7 with increasing temperature (see table 3). This indicates a considerable anisotropy of growth, resulting in spiky crystals (bundle-like or sheaf-like crystallites) for slow heating rates and isotropic growth upon fast heating [4].

Table 3. Non-isothermal cold crystallization kinetics parameters of 5P-Am*FLAm*-P5 obtained from the Ozawa analyses.

Ozawa model		
T (K)	n_O	$\log(Z$ (K/min))
301	6.3 ± 0.9	5.8 ± 0.9
305	5.3 ± 0.3	5.1 ± 0.4
307	4.6 ± 0.1	4.7 ± 0.2
311	4.1 ± 0.1	4.7 ± 0.1
313	3.9 ± 0.1	4.7 ± 0.1
316	3.7 ± 0.1	4.9 ± 0.2

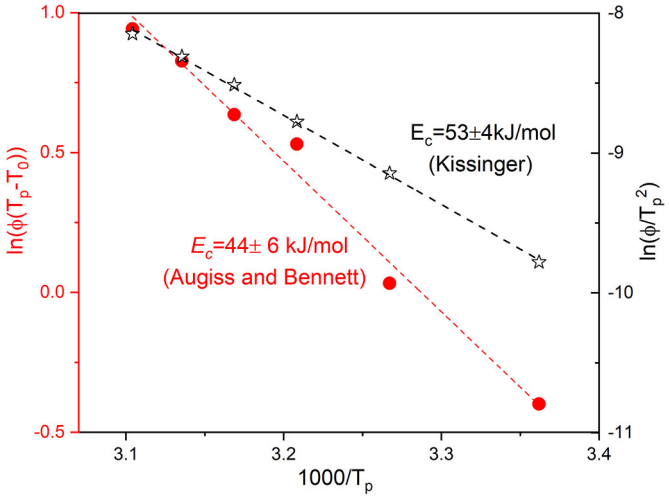

Fig. 10. Kissinger (open symbol) and Augiss and Bennett (full symbol) plots for non-isothermal cold crystallization of Cr2 in 5P-Am*FLAm*-P5.

The activation energy (E_c) necessary to be overcome during the non-isothermal crystallization process was approximated using an equation proposed by Kissinger [45]:

$$\ln \frac{\phi}{T_p^2} = C - \frac{E_c}{RT_p} \qquad (11)$$

and by Augiss and Bennett [46]:

$$\ln \frac{\phi}{T_p - T_0} = C_{AB} - \frac{E_c}{RT_p}, \qquad (12)$$

where C and C_{AB} denote fitting parameters, ϕ indicates cooling/heating rate, T_p is the maximum crystallization peak and T_0 indicates the onset temperature of crystallization. The analysis of non-isothermal crystallization data in terms of eqs. (11) and (12) is presented in fig. 10. The activation energy thus obtained from the Kissinger equation ($E_c = 53 \pm 4$ kJ/mol), is in agreement with that of the Augiss and Bennett approach ($E_c = 44 \pm 6$ kJ/mol),

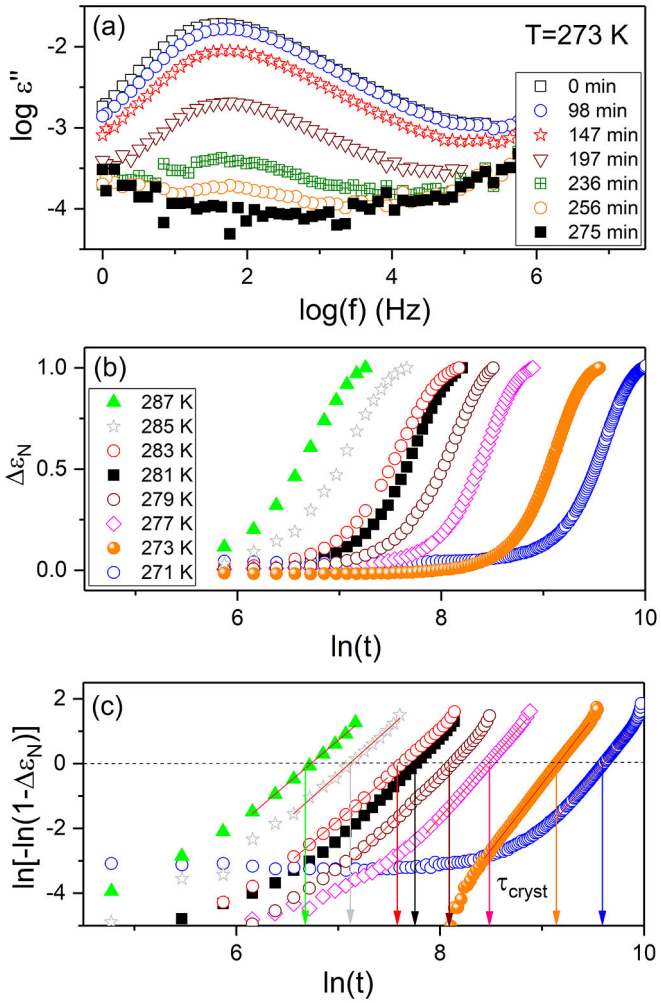

Fig. 11. (a) Dielectric loss spectra measured during isothermal cold crystallization of Cr2 in 5P-Am*FLAm*-P5 at 273 K. (b) Time evolution of the normalized dielectric strength $\Delta\varepsilon_N$ during isothermal cold crystallization. (c) Avrami plot of $\Delta\varepsilon_N$ for the data presented in panel (b). The values of τ_{cryst} were determined for $\ln[-\ln(1-\Delta\varepsilon_N)] = 0$.

within the limits of error. The small difference between the observed values is due to the fact that unlike eq. (12), eq. (11) does not take into account the onset temperature of crystallization.

3.4 Kinetics of cold crystallization of Cr2 in 5P-Am*FLAm*-P5 under isothermal conditions

To observe the kinetics of isothermal cold crystallization of Cr2 in 5P-Am*FLAm*-P5, the sample was first cooled to a glass N* state, then heated to a selected temperature (271 K, 273 K, 277 K, 279 K, 281 K, 283 K, 285 K, 287 K). The time evolution of dielectric spectra at 273 K is presented in fig. 11(a). An increase of the crystalline fraction (ε_N) (see fig. 11(b)) can be obtained from an analysis of dielectric loss spectra: any reduction of molecular mobility is reflected as a gradual decrease of the peak amplitude

Table 4. Parameters of the kinetics of the Cr2 crystallization process in 5P-Am*FLAm*-P5 obtained from the analysis of BDS data by means of the Avrami model.

T [K]	n	$\ln K$	$\ln \tau_{cr}$
271	3.7 ± 0.1	-35.8 ± 0.1	9.6 ± 0.1
273	4.0 ± 0.1	-37.2 ± 0.1	9.1 ± 0.1
277	$3.6 + 0.1$	-30.5 ± 0.5	8.5 ± 0.4
279	$3.1 + 0.3$	-25.3 ± 2.0	8.1 ± 0.9
281	$3.2 + 0.1$	-25.1 ± 0.5	7.8 ± 0.4
283	$2.9 + 0.1$	-21.7 ± 1.0	7.6 ± 1.1
285	$2.8 + 0.1$	-20.1 ± 0.5	7.1 ± 0.3
287	$2.8 + 0.1$	-18.1 ± 0.5	6.7 ± 0.4

and the dielectric strength ($\Delta\varepsilon = \varepsilon_s - \varepsilon_\infty$, where ε_s and ε_∞ are values of the real part ε' in the limit of low and high frequency, respectively). By following the changes in $\Delta\varepsilon$ ε_N is found as

$$\varepsilon_N = \frac{\Delta\varepsilon(0) - \Delta\varepsilon(t)}{\Delta\varepsilon(0) - \Delta\varepsilon(\infty)}, \tag{13}$$

where $\Delta\varepsilon(0)$, $\Delta\varepsilon(t)$ and $\Delta\varepsilon(\infty)$ are the values of the dielectric strength at the beginning of the observation, at time t and at the end. The kinetics of isothermal crystallization of 5P-Am*FLAm*-P5 was analyzed by the Avrami model

$$\Delta\varepsilon_N(t) = 1 - \exp(-Kt^{n_A}), \tag{14}$$

where $K = k^{n_A}$ is a constant depending on the crystallization temperature and geometry of the sample and n_A is the Avrami exponent. The characteristic time of crystallization $\tau_{cryst} = K^{-1/n}$, defined as the time needed to achieve 63% of the final crystallinity, was designated based on eq. (14) presented in the logarithmic form, *i.e.* $\ln[-\ln(1-\Delta\varepsilon_N)]$ *vs.* $\ln(t)$ (fig. 11(c)). As a result, straight lines were obtained, with n_A being the slope and $\ln K$ the intercept with the y-axis. The fact that n_A changes from 4 to 2.8 with increasing temperature (see table 4) suggests the presence of a spherical three-dimensional crystal growth [4]. The activation energy of isothermal cold crystallization in metastable nematic ($E_c \approx 114$ kJ/mol), determined from the obtained slope of temperature dependence $\ln(\tau_{cryst})$ (fig. 12), is more than twice as large as that required for the non-isothermal cold crystallization process in the isotropic phase. This can be attributed to the lower viscosity of the material in the liquid than the nematic state, which facilitates molecular diffusion.

Figure 12(b) shows the dependence between molecular mobility and crystallization rate. The extent of the correlation between the α-relaxation times (τ_α) and the characteristic time of crystallization (τ_{cryst}), designated as the slope of τ_α *vs.* τ_{cryst}, equals 0.52. This finding coincides well with the value obtained from the relationship between the coupling coefficient ξ and the fragility m_f, defined by

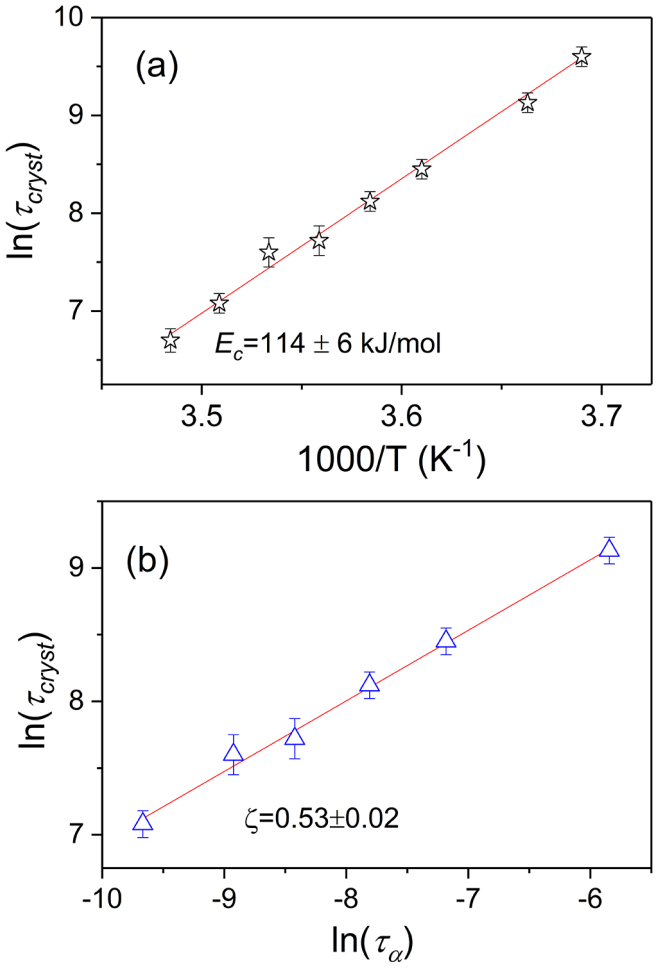

Fig. 12. (a) Characteristic crystallization time (τ_{cryst}) *vs.* reciprocal temperature for isothermal cold crystallization of Cr2 in the N* state. (b) The characteristic crystallization time (τ_{cryst}) as a function of the α-relaxation time (τ_α).

Ediger as $\xi = 1.1 - 0.005 m_f$. With regard to Jackson's criterion of type-A melt/crystal interfaces, a large entropy of fusion ($\Delta_m S_{\text{Cr2-}I} \approx 68\,\text{J mol}^{-1}\text{K}^{-1}$, $> 4R$; R: a gas constant) indicates a flat melt/crystal interface growing laterally.

4 Conclusions

The molecular dynamics and crystallization behavior of glass-forming chiral-nematic 5P-Am*FLAm*-P5 liquid crystal were studied under various thermal conditions by a combination of BDS, POM and DSC methods. As the sample was cooled slowly, the isotropic state was found to form a conformationally disordered Cr1 phase (condis) which then vitrified (Is-Cr1-GCr1). On heating, the glass state was seen to soften, and fusion of Cr1 was observed (GCr1-Cr1-Is). In contrast, fast cooling ($\phi \geq 5\,\text{K/min}$) resulted in the vitrification of the N* phase (Is-N*-GN*); upon subsequent heating, after softening of the glass, the metastable nematic phase became an isotropic phase and then crystallized to Cr2, before finally melting (GN*-N*-Is-Cr2-Is). The fact that melting entropy values of the Cr1 and Cr2 crystals were comparable suggests that the two phases have similar degrees of order. The vitrification of N* is accompanied by a super-Arrhenius–type structural α-relaxation. The relaxation processes observed in the Cr1 and Cr2 phases related to the small twisting movements of fluorene groups are Arrhenius like. The activation energy ($E_c \approx 114\,\text{kJ/mol}$) calculated for the isothermal cold crystallization process of Cr2 occurring in the metastable N* phase is twice that of the value estimated for the non-isothermal experiments ($E_c \approx 44\,\text{kJ/mol}$): in these, the Cr2 crystallization occurs in the isotropic phase obtained upon heating the metastable N* phase. This is attributed to the fact that the isotropic state facilitates the transport of molecules across the phase boundary. For slow heating rates, the growth rate of Cr2 demonstrated considerable anisotropy; in contrast, isotropic growth was observed upon fast heating and in isothermal experiments.

Finally, further conclusions can be drawn by comparing our present findings for 5P-Am*FLAm*-P5 with those obtained previously for a non-chiral 5P-EtFLEt-P5 compound [23] composed of molecules with the same core. i) 5P-EtFLEt-P5 shows a very strong tendency to vitrification in the N phase, even upon cooling at rates as low as 0.1 K/min; it then follows the sequence GN-N-Cr1-Cr2-Is upon heating. In contrast, the phase behavior of 5P-Am*FLAm*-P5 is strongly dependent on cooling rate. ii) The crystals formed by non-chiral molecules of 5P-EtFLEt-P5 are characterized by a higher degree of order than those found in 5P-Am*FLAm*-P5, as evidenced by the entropy of fusion. iii) The crystallization rates of isothermal cold crystallization of Cr1 in N phase in 5P-EtFLEt-P5 were found to be controlled by kinetic factors at low temperatures and thermodynamic factors at high temperature. Conversely, in the case of cold crystallization of Cr2 in the N* phase for 5P-Am*FLAm*-P5, the observed molecular dynamics were more decisive for all tested temperatures. iv) The value of activation of the energy of the isothermal cold crystallization in the N* phases ($E_c \approx 114\,\text{kJ/mol}$) is comparable with the value obtained for the parallel process in the N phase in the vicinity of T_g ($E_c \approx 100\,\text{kJ/mol}$). According to Jackson's criterion, both materials show a flat melt/crystal interface growing laterally by either screw dislocation or surface nucleation growth.

MJ-D acknowledges the National Science Centre (Grant SONATA11: UMO-2016/21/D/ST3/01299) for financial support.

Author contribution statement

MJ-D defined the conception of studies, performed BDS measurements, analyzed the kinetics of non-isothermal crystallization process based on DSC data, and led the writing of the manuscript; TR carried out the POM measurements and simulations of the structures of investigated

molecules; EJ-G carried out DSC measurements and thermogram analysis; JK wrote the software for BDS data analysis; ED and PK synthesized the investigated LC material; M-M-A analyzed the BDS data, participated in the preparation of the manuscript. All authors discussed the results and approved the final version of the manuscript.

References

1. L.S. Taylor, in *Pharm Sci Encycl* (John Wiley & Sons, Inc., Hoboken, NJ, USA, 2015) pp. 1–39.
2. S. Andjelić, R.C. Scogna, J. Appl. Polym. Sci. **132**, 42066 (2015).
3. Y.H. Roos, Annu. Rev. Food Sci. Technol. **1**, 469 (2010).
4. J.W.P. Gutzow, S. Ivan, Schmelzer, *The Vitreous State: Thermodynamics, Structure, Rheology, and Crystallization*, second edition (Springer Berlin Heidelberg, 1995).
5. K. Koperwas, K. Adrjanowicz, Z. Wojnarowska, A. Jedrzejowska, J. Knapik, M. Paluch, Sci. Rep. **6**, 36934 (2016).
6. D.L. Leslie-Pelecky, N.O. Birge, Phys. Rev. B **50**, 13250 (1994).
7. P. Supaphol, J.E. Spruiell, Polymer **42**, 699 (2001).
8. K. Iwase, Y. Nagano, I. Yoshikawa, H. Houjou, Y. Yamamura, K. Saito, J. Phys. Chem. C **118**, 27664 (2014).
9. M. Jasiurkowska-Delaporte, T. Rozwadowski, E. Juszyńska-Gałązka, Crystals **9**, 205 (2019).
10. P.G. Debenedetti, F.H. Stillinger, Nature **410**, 259 (2001).
11. M.D. Ediger, C.A. Angell, S.R. Nagel, J. Phys. Chem. **100**, 13200 (1996).
12. C.A. Angell, Science **267**, 1924 (1995).
13. K. Ito, C.T. Moynihan, C.A. Angell, Nature **398**, 492 (1999).
14. L.-M. Martinez, C.A. Angell, Nature **410**, 663 (2001).
15. N.A. Mauro, M. Blodgett, M.L. Johnson, A.J. Vogt, K.F. Kelton, Nat. Commun. **5**, 4616 (2014).
16. J. Mayer, J. Krawczyk, M. Massalska-Arodź, I. Natkaniec, J.A. Janik, O. Steinsvoll, Physica B: Condens. Matter **371**, 249 (2006).
17. H. Shintani, H. Tanaka, Nat. Phys. **2**, 200 (2006).
18. M.D. Ediger, P. Harrowell, L. Yu, J. Chem. Phys. **128**, 034709 (2008).
19. E.-J. Donth, *The Glass Transition* (Springer Berlin Heidelberg, Berlin, Heidelberg, 2001).
20. R. Brand, P. Lunkenheimer, A. Loidl, J. Chem. Phys. **116**, 10386 (2002).
21. M. Sorai, S. Seki, Mol. Cryst. Liq. Cryst. **23**, 299 (1973).
22. M. Massalska-Arodź, G. Williams, I.K. Smith, C. Conolly, G. Anthony Aldridge, R. Dabrowski, J. Chem. Soc. Faraday Trans. **94**, 387 (1998).
23. M. Jasiurkowska-Delaporte, T. Rozwadowski, E. Dmochowska, E. Juszyńska-Gałązka, P. Kula, M. Massalska-Arodź, J. Phys. Chem. B **122**, 10627 (2018).
24. M. Jasiurkowska, J. Ściesiński, J. Czub, M. Massalska-Arodź, R. Pełka, E. Juszyńska, Y. Yamamura, K. Saito, J. Phys. Chem. B **113**, 7435 (2009).
25. M. Jasiurkowska-Delaporte, M. Massalska-Arodź, J. Mol. Liq. **241**, 355 (2017).
26. M. Jasiurkowska, P.M. Zieliński, M. Massalska-Arodź, Y. Yamamura, K. Saito, J. Phys. Chem. B **115**, 12327 (2011).
27. R. Pełka, Y. Yamamura, M. Jasiurkowska, M. Massalska-Arodź, K. Saito, Liq. Cryst. **35**, 179 (2008).
28. M. Jasiurkowska-Delaporte, S. Napolitano, J. Leys, E. Juszyńska-Gałązka, M. Wübbenhorst, M. Massalska-Arodź, J. Phys. Chem. B **120**, 12160 (2016).
29. E. Juszyńska, M. Jasiurkowska, M. Massalska-Arodź, D. Takajo, A. Inaba, Mol. Cryst. Liq. Cryst. **540**, 127 (2011).
30. G.P. Johari, J.W. Goodby, J. Chem. Phys. **77**, 5165 (1982).
31. M. Cocca, R. Androsch, M.C. Righetti, M. Malinconico, M.L. Di Lorenzo, J. Mol. Struct. **1078**, 114 (2014).
32. N. Osiecka, E. Juszyńska-Gałązka, Z. Galewski, T. Jaworska-Gołąb, A. Deptuch, M. Massalska-Arodź, J. Therm. Anal. Calorim. **133**, 961 (2018).
33. T. Rozwadowski, M. Massalska-Arodź, Ł. Kolek, K. Grzybowska, A. Bąk, K. Chłędowska, Cryst. Growth Des. **15**, 2891 (2015).
34. M. Jasiurkowska-Delaporte, E. Juszyńska, Ł. Kolek, J. Krawczyk, M. Massalska-Arodź, N. Osiecka, T. Rozwadowski, Liq. Cryst. **40**, 1436 (2013).
35. K. Kolodziejczyk, K. Grzybowska, Z. Wojnarowska, M. Dulski, L. Hawelek, M. Paluch, Cryst. Growth Des. **14**, 3199 (2014).
36. Ł. Kolek, M. Massalska-Arodź, D. Majda, B. Suchodolska, S. Zalewski, Acta. Phys. Pol. A **124**, 909 (2013).
37. M. Descamps, E. Dudognon, J. Pharm. Sci. **103**, 2615 (2014).
38. M. Wübbenhorst, J. Van Turnhout, J. Non-Cryst. Solids **305**, 40 (2002).
39. F. Meersman, B. Geukens, M. Wübbenhorst, J. Leys, S. Napolitano, Y. Filinchuk, G. Van Assche, B. Van Mele, E. Nies, J. Phys. Chem. B **114**, 13944 (2010).
40. R.P. Sharma, P.F. Green, Macromolecules **50**, 6617 (2017).
41. S. Madkour, P. Szymoniak, J. Radnik, A. Schönhals, ACS Appl. Mater. Interfaces **9**, 37289 (2017).
42. H.W. Starkweather, P. Avakian, J. Polym. Sci. Part B: Polym. Phys. **30**, 637 (1992).
43. D.W. Henderson, J. Non-Cryst. Solids **30**, 301 (1979).
44. T. Ozawa, Polymer **12**, 150 (1971).
45. H.E. Kissinger, J. Res. Natl. Bur. Stand. **57**, 217 (1956).
46. J.A. Augis, J.E. Bennett, J. Therm. Anal. Calorim. **13**, 283 (1978).